6 Particle Physics with CMS at LHC

C. Amsler, V. Chiochia, A. Dorokhov, C. Hörmann, K. Prokofiev, H. Pruys,
C. Regenfus, P. Robmann, T. Speer, and S. Steiner

in collaboration with:
ETH-Zürich, Paul Scherrer Institut (PSI), Universität Basel and the CMS Collaboration.

(CMS Collaboration)

During 2003 our group continued to design and test the pixel sensors and readout chips for the innermost vertex detector of the CMS experiment. We are also involved in the charged particle reconstruction software and the workshop of our institute is developing the support structure and service tube for the pixel detector.

The CMS (Compact Muon Solenoid) at the Large Hadron Collider (LHC) will start operating at CERN in 2007. Our group will concentrate on physics involving the b- and t-quarks quark, e.g. b-quark production associated with the formation of Higgs bosons. The most interesting events at LHC will contain one or several b-jets originating from the decay of B mesons, with typical decay lengths of a few mm. To allow for efficient tagging of B mesons among the large background of light quark and gluon jets, the detection system has to trace back particles towards the primary vertex. The silicon pixel detector we are developing is the closest detector to the interaction point, located only 4 cm from the beam-beam interaction point. The extremely high particle flux near the primary vertex ($\approx$ 1000 particles every 25 ns) requires the innermost tracking layers to be composed of pixel devices delivering 3D coordinates with high resolution and no ambiguity.

The barrel pixel detector consists of three concentric cylindrical layers, 53 cm long with radii of 4.4, 7.3 and 10.2 cm. The layers contain some 3×10^7 silicon pixels. The pixel modules consist of thin, segmented sensor plates with highly integrated readout chips connected by indium bump bonds (Fig. 6.1). The final pixel size will be $100 \times 150\,\mu\mathrm{m}^2$. The analogue signals are read out to determine the coordinates more accurately, using charge sharing between adjacent pixels.

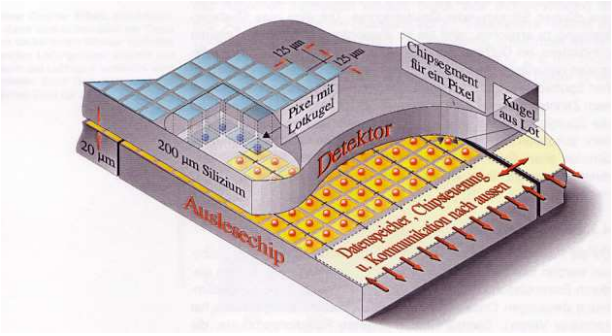

Figure 6.1: *Schematic view of a pixel detector element. Each sensor pixel is connected through an indium solder bump to a pixel unit cell on the readout chip which amplifies and processes the signal. The data are stored on the edge of the chip where they wait for trigger confirmation.*

6.1 Development of pixel sensors

The CMS pixel sensors are manufactured using the "n-on-n" technique consisting of n^+-structures on n-bulk silicon. This allows the partially depleted operation of highly irradiated sensors after type inversion, but also requires inter-pixel isolation. Two isolation techniques were considered for our

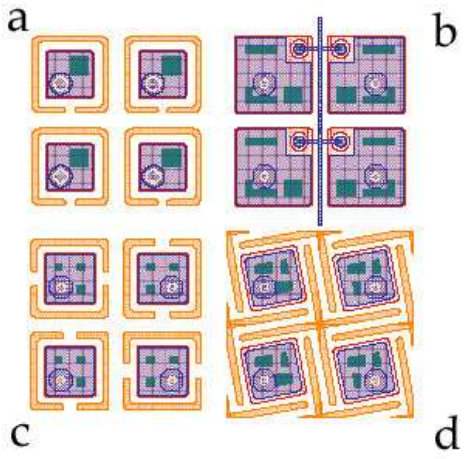

Figure 6.2: *Some of our favorite designs for the pixel sensors. Open p-stop rings (a and c), p-stop crosses (d) and p-spray with bias grid (b).*

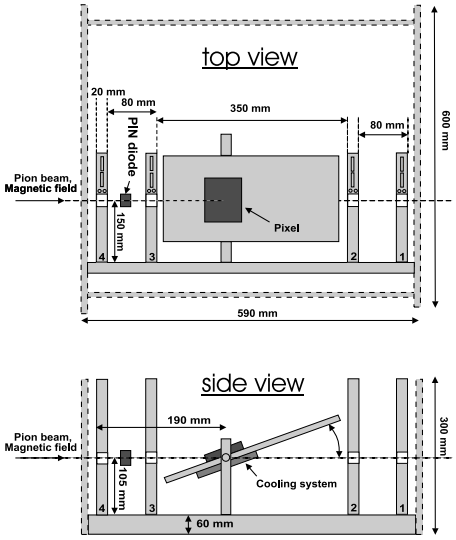

Figure 6.3: *Top and side views of the beam telescope.*

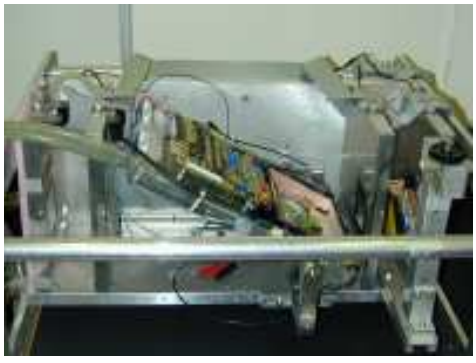

Figure 6.4: *Beam telescope setup.*

latest prototypes: p-spray [1], for which a uniform average dose of p-impurities ($\approx 10^{12}$ cm^{-2}) covers the whole structured surface, and p-stop rings ($\approx 10^{13}$ impurities cm^{-2}) which surround the n^+-implants (Fig. 6.2). Possible failures of the pixel bump-bonds require a method to evacuate the charge. This is achieved with a bias grid and punch-through structures for the p-spray detectors and by openings in the rings for the p-stop detectors.

Test measurements were performed in the H2 beam line of the CERN SPS in June and September 2003 using 150-225 GeV pions. The test devices contained 22×32 pixels with a total sensitive area of 2.75×4 mm^2, and a thickness of 280 μm. The readout pitch was still of the old design, 125 μm $\times$ 125 μm. Some of these devices had been previously irradiated in a 24 GeV proton beam at the CERN PS. The sensors received total particle fluences of 3.3×10^{14} n_{eq}/cm^2, 8.1×10^{14} n_{eq}/cm^2 and 1.1×10^{15} n_{eq}/cm^2. They were bump bonded to non-irradiated readout chips of the DMILL type.

The hit coordinates in the pixel detector were determined accurately with our silicon reference telescope [2]. The beam telescope consisted of 4 modules, each with two orthogonal 300μm thick single-sided silicon detectors (32×30 mm^2) with a strip pitch of 25 μm and a readout pitch of 50 μm. The resulting intrinsic resolution of the beam telescope was around σ = 1 μm.

The pixel sensor with the readout chip was mounted on a rotating support positioned between the second and the third module (Figs. 6.3 and 6.4). A trigger signal was generated by a PIN diode. The data acquisition system and slow control (temperature and bias voltage) were written in LabView and LabWindows CVI (National Instruments) running on a PC. The analog signals were digitized in a VME based readout system by FADCs. The setup was located in an open 3 T Helmholtz magnet with magnetic field parallel to the beam. The pixel sensors were cooled with water cooled Peltier elements. Similar measurements were performed earlier by our group [3; 4] but irradiated sensors could not be tested reliably because they were not cooled down to the -10° C foreseen for the CMS tracker. A more detailed discussion of the latest beam test results can be found in ref. [8].

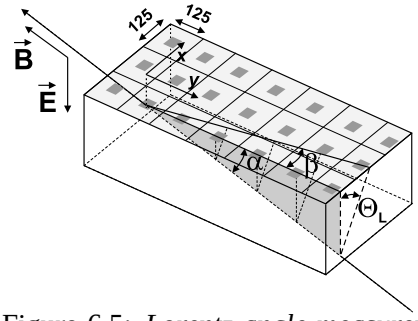

Figure 6.5: *Lorentz angle measurement with the grazing angle method.*

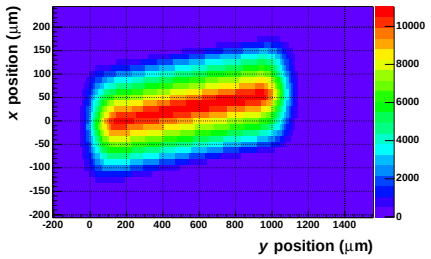

Figure 6.6: *Deflection of the drifting charge in a 3 T magnetic field.*

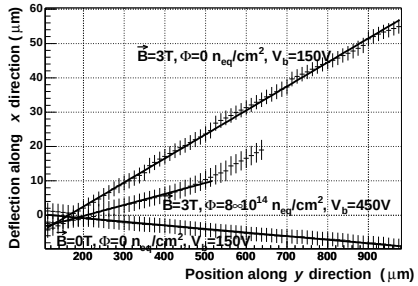

Figure 6.7: *Deflection of the collected charge as a function of the y-position. The solid line is the fit.*

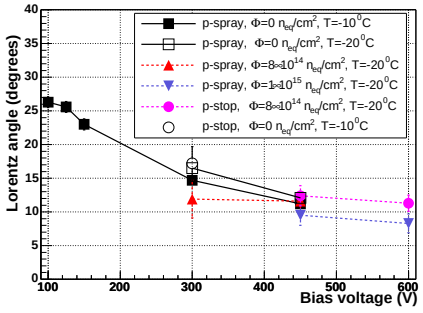

Figure 6.8: *Lorentz angle as a function of bias voltage for a magnetic field extrapolated to 4 T.*

6.1.1 Lorentz angle measurements

The Lorentz angle was obtained by the direct measurement of the charge drift in the magnetic field using the grazing angle method [4]. The pion beam which was in direction of the magnetic field entered the sensor surface at a shallow angle $\alpha = 15°$ (Fig. 6.5). The deposited charge drifts according to the combined electric and magnetic forces, resulting in a deflection of the particle track projection on the surface by the angle β from which the Lorentz angle Θ_L could be obtained. The deflection observed at 3 T magnetic field is illustrated in Fig. 6.6 for the non-irradiated p-spray sensor.
The angle β was measured by slicing the histogram perpendicularly to the y-axis. The x position of the charge center is shown in Fig. 6.7 as a function of y. A measurement without magnetic field is used to correct for detector misalignment with respect to the beam (bottom line). For the irradiated device there are two regions with different slopes, and hence two different Lorentz angles. This behaviour can be explained by the non-linear behaviour of the electric field in the irradiated devices (see next section). Since most of the signal charge is collected from the region close to the pixel implant, this region was used to determine the Lorentz angle.
Figure 6.8 shows the measured Lorentz angles for non-irradiated and irradiated sensors, extrapolated to 4 T. One observes a strong dependence of the Lorentz angle on the bias electric field, which is weakly affected by irradiation and does not depend strongly on sensor design. For the non-irradiated sensors a Lorentz angle of $26°$ can be reached at a bias voltage of 100 V, while irradiated sensors have to be operated at much higher bias voltages, where the Lorentz angle drops to roughly $10°$. Our results are in a good agreement with other measurements and simulations [5].

6.1.2 Charge collection in irradiated sensors

Following irradiation, the amount of collected charge decreases due to charge trapping and partial depletion of the sensor. Measurements of the charge collection efficiency as a function of sensor depth were performed using the grazing angle method, this time with magnetic field off. The charge collected in non-irradiated and irradiated p-spray sensors as a function of depth is shown in Fig. 6.9. In the non-irradiated sensor the charge is collected uniformly across the whole sensor depth, while

the irradiated devices exhibit a different behaviour. At low bias voltages charge is also collected from the side opposite to the pixel implants which could indicate that the depletion starts from both sides of the detector, due to the non-linear behaviour of the electric field. The fraction of collected charge for different designs and irradiation doses is shown in Fig. 6.10 as a function of bias voltage. Charge collection also depends on the position of the incident particle with respect to the pixel implant since the gaps between pixels have a reduced sensitivity. The average charge collected is shown in Fig. 6.11 as a function of position for non-irradiated and irradiated sensors. The signal-to-noise ratio decreases from 65 to 35 after irradiation. Thus the CMS pixel detector will operate up to the maximum expected irradiation dose. Note that the area with reduced charge collection between pixels is larger for the p-stop design.

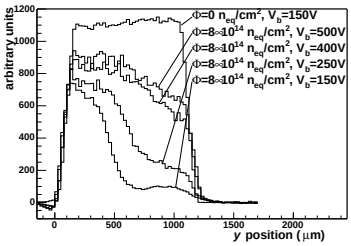

Figure 6.9: *Charge collected for different bias voltages.*

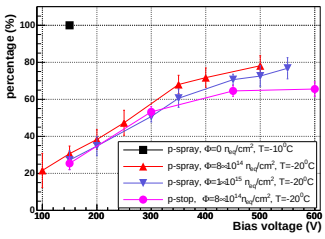

Figure 6.10: *Total collected charge normalized to non-irradiated device.*

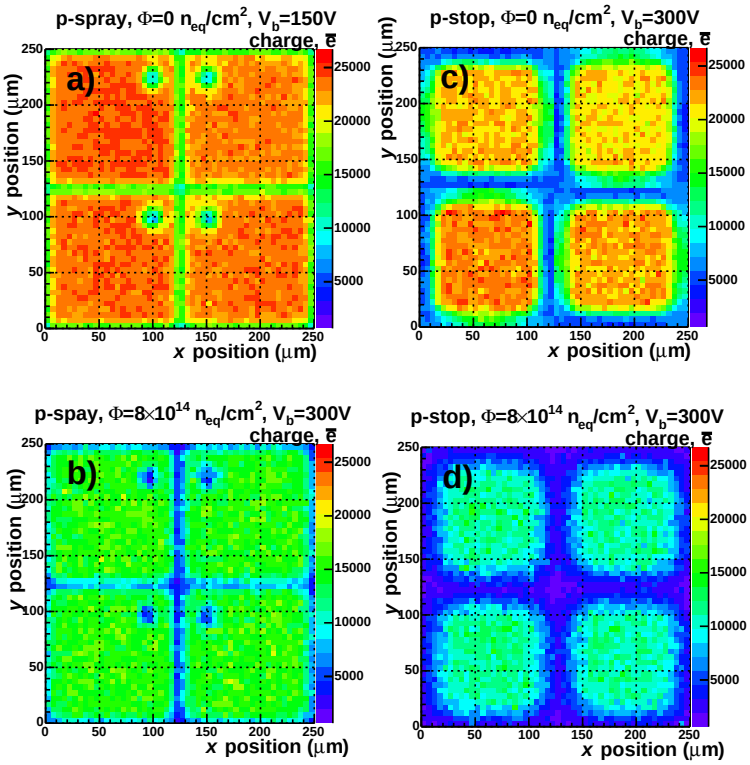

Figure 6.11: *Distribution of charge collected in the pixels. The top plots show the non-irradiated p-spray (a) and p-stop designs (c), the bottom plots the respective irradiated sensors.*

6.2 Development of the pixel readout chip

We collaborate with PSI in the design of the readout chip (ROC) [6]. The prototype (PSI46) in quarter micron technology DSM (Deep Sub Micron) was submitted and delivered by the manufacturer in 2003. The previous chips had been processed in radiation hard DMILL technology. DSM technology is a well known standard process, significantly cheaper than DMILL which was especially developed for radiation hard devices. However, DSM designs can also be radiation hard. We expect a better yield with DSM than with DMILL and, indeed, the preliminary yield is 80% for DSM, compared with 20% for our previous DMILL chips (PSI43). Power consumption is also lower in DSM which requires only half of the supply voltage and half of the current, hence a quarter of the total power consumption.

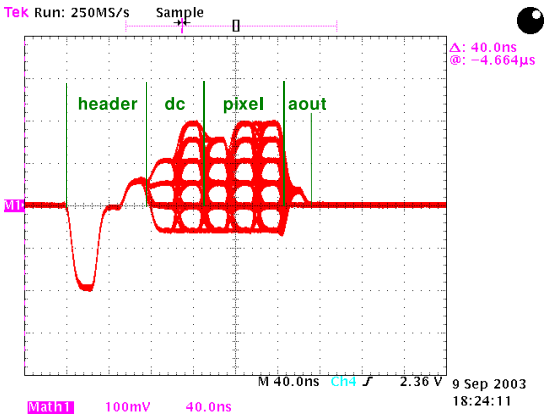

Figure 6.12:
Event readout structure of PSI46 (see text).

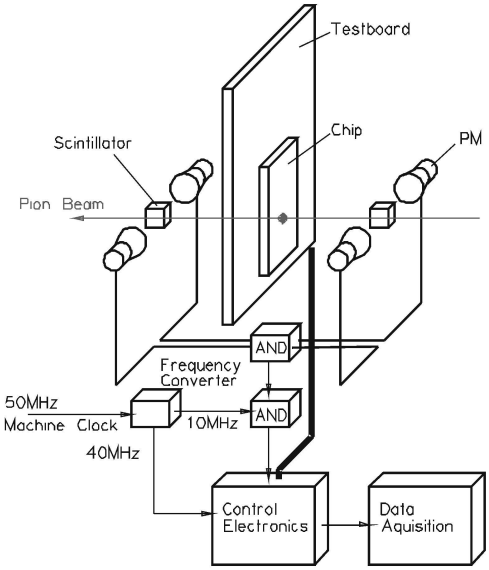

Figure 6.13: *Test beam setup.*

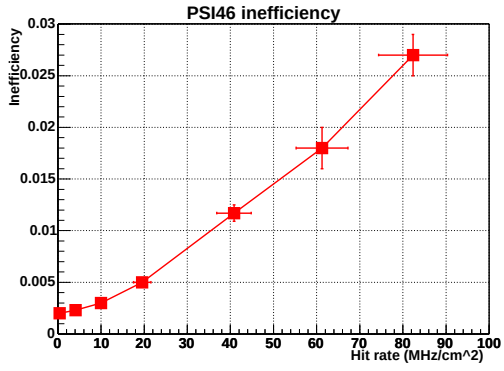

Figure 6.14: *Data loss measured with test pions.*

DSM technology also offers new possibilities in designing chips and improving their performances. There are five metal layers available for routing instead of only two, and the smallest feature size is 0.25 μm, compared to 0.8 μm for DMILL. Hence more complex circuits can be designed to cope with the updated requirements at LHC: the three layers of pixel detectors will now be operated at high luminosity, including the innermost at 4 cm from the interaction vertex. In DMILL technology, however, we would have an unacceptable fraction of lost data.

The wafer submitted to the manufacturer in 2003 contained four versions of the ROC which differ essentially in the power decoupling scheme (to minimize cross talk and therefore allow lower comparator thresholds) and the total area of metal insulator metal capacitors. Test circuits for internal measurements at points that are not accessible in the ROC were also foreseen in the wafer. In particular, we designed a circuit to investigate single event upsets, see below.

The analog readout of the ROC was tested in the laboratory (Fig. 6.12). The first three cycles are used for the header, the next two for the double column address and the following three for the pixel addresses. The addresses are coded by six analog levels which are clearly distinguishable in Fig. 6.12. The last cycle is the analog pulse height. The cycles for the address of the double column, the pixel address and the pulse height are repeated for each hit. The readout frequency is 40 MHz.

The ROC was tested on the 300 MeV/c πE_1 beamline at PSI. One of the goals was to investigate the data loss under LHC equivalent intensities. The beam intensity varied up to 8×10^7 pions/cm^2 which corresponds to the expected track density at CMS for the middle layer of the pixel detector. The experimental layout is shown in Fig. 6.13. The trigger signal was generated by scintillators and reduced to 10 kHz by coincidence with the random signal of a radioactive source. The ROC was operated with a synchronized 40 MHz frequency which corresponds to the bunch crossing frequency at LHC.

The inefficiency versus fluence is shown in Fig. 6.14. The data loss of PSI46 (2.5 % at the maximum luminosity) is about an order of magnitude smaller than that of PSI43, but still some-

what higher than expected. Hence the translation of the ROC from DMILL to DSM was successful and the new chip is much more performant. Some minor improvements are, however, still necessary.

Single event upsets (SEU) occur during high energy deposits in a small sensitive volume of the electronics circuit, leading to unwanted bit flips. SEU events are due to hadronic interactions with nuclei on the lattice. This is a known problem, e.g. in space applications, which has also to be taken seriously at LHC. SEU is more dangerous in DSM technology due to smaller node capacities, faster circuits and lower supply voltages, and is a serious problem for detector control functions. For example, the analog converter values and trimbits for the thresholds are stored in memory cells. In order to deal with the SEUs, one has to reload permanently the storage cells, which causes unnecessary data traffic.

In our measurements we investigated the effects of capacitors as protections against SEUs. The SEU test structures designed in DSM technology consisted of shift registers protected by capacitors. The shift registers were filled with 1 or 0 and read out every 5 minutes to count the flipped bits. The cross sections for bit flips are shown in figure 6.15 as a function of supply voltage. The cross sections for SEU are roughly two orders of magnitude smaller with protective capacitor.

Another interesting result is the asymmetry in the probabilities for 1 to 0 flips and 0 to 1 flips. The ratio of probabilities $0 \rightarrow 1 \,/\, 1 \rightarrow 0$ is about 120. Figure 6.16 shows the spatial distribution of SEUs after 160 readouts of 5 minutes each, at a supply voltage of 1.5 V. The upper row shows the spatial distribution of SEUs in the unprotected shift registers and the lower row shows the distribution for the protected cells.

By histogramming the number of SEUs after each readout one obtains a Poisson distribution. This is a hint for independent single pixel upsets and no clusterisation of SEUs. The ratio of SEU cross sections for π^+/π^- is 1.6. The ratio for π^+/p (~ 5) was also measured using 500 MeV/c protons. This is an important measurement since most investigations for space applications were done with protons.

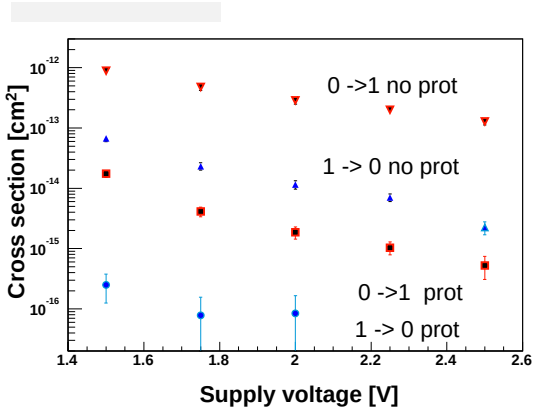

Figure 6.15: *SEU cross sections for 300 MeV/c π^+ on the SEU test structures for various supply voltages.*

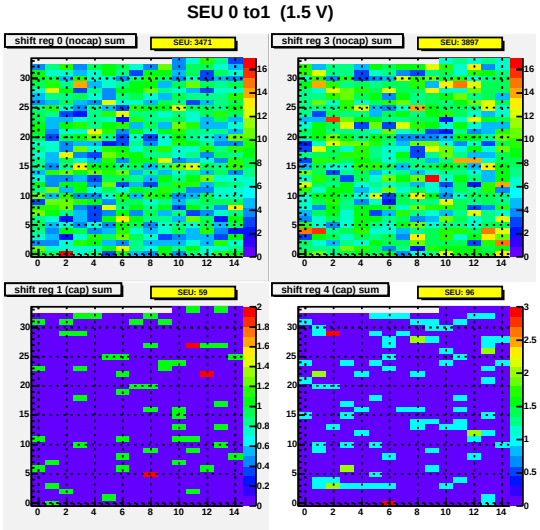

Figure 6.16: *Accumulated spatial distribution of SEUs after 160 readouts for four shift registers in parallel. The upper row shows the distribution of two unprotected shift registers and the lower one the distribution for two protected shift registers.*

6.3 Event reconstruction software

We are developing techniques to reconstruct the interaction vertex in CMS within the object-oriented reconstruction framework (ORCA). After having implemented in ORCA a single-vertex fit algorithm using the Kalman filter formalism (see last year's annual report and ref. [7]), we are now developing an algorithm based on a the so-called Gaussian sum filter.

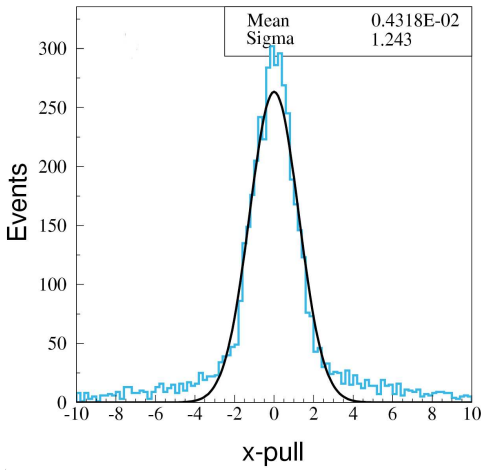

Figure 6.17: *Pull of the reconstructed vertex x-coordinate.*

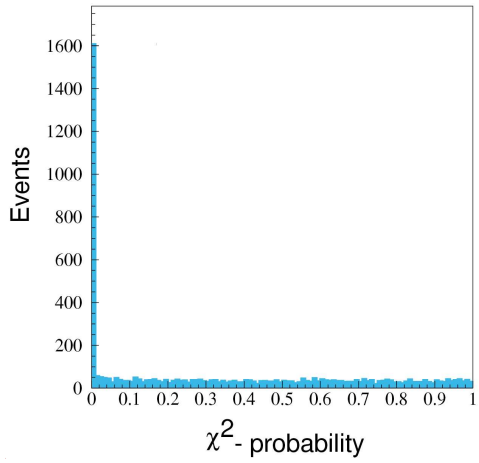

Figure 6.18: *χ^2-probability distribution for the Kalman filter.*

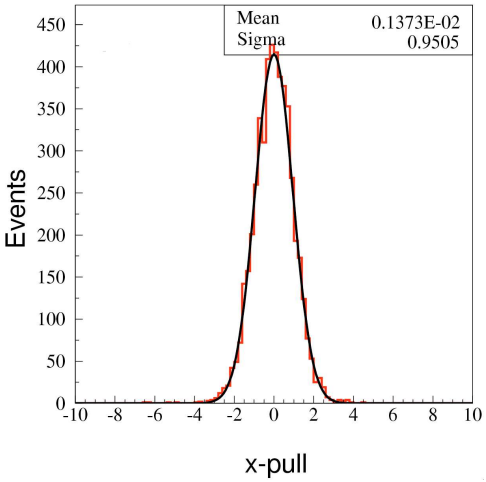

Figure 6.19: *Pull of the reconstructed vertex x-coordinate.*

The usual vertex reconstruction algorithm is the Kalman filter based on a least square minimization, which hence assumes that the track measuring errors follow a normal distribution. However, a non-Gaussian noise (due e.g. to δ-electrons) is always present. One method that takes non-Gaussian effects into account is the Gaussian-sum filter (GSF) in which the measurement errors are modeled by a superposition of several (mostly two) Gaussians which we shall refer to as *components*. It is a non-linear estimator, in which the weights of the components depend on the measurements.

In an iterative procedure, the estimate of the vertex is updated with one track at the time. The vertex consists of several solutions calculated with all possible components of the tracks. When one track is added to the vertex, each solution for the vertex is combined with each component of the new track, using the Kalman filter. The final vertex estimate is then calculated as the weighted average of all solutions. Since the number of solutions increases exponentially, it has to be limited to an acceptable number. This is achieved by merging solutions which are close enough.

To investigate the performance of a such an algorithm we made a simulation using vertices leading to four-tracks. No track reconstruction was performed but track parameters were smeared according to a two-component Gaussian model. The component modeling the non-Gaussian tails had a standard deviation ten times larger than that of the core component and their relative weights were 9:1.

For a fit with the Kalman filter, for which only one component is used, the distributions of the vertex pulls (difference between simulated and reconstructed values divided by the measurement error) show a Gaussian core with tails (Fig. 6.17) and a large fraction of the fitted events have a very small χ^2-probability (Fig. 6.18).

In the GSF method the two components are used, each with the correct weight and variance. The pulls have a resolution closer to unity when fitted with a Gaussian, the tails vanish (Fig. 6.19) and the peak at low χ^2 disappears (Fig. 6.20). This indicates that the error estimates and component weights were reasonable. These encouraging tests demonstrate the power of the algorithm and its efficiency in the presence of non-Gaussian noise.

We are also developing a kinematic fit using the Lagrange multiplier method which incorporates additional constraints into the vertex fit. Additional constraints such as masses of decaying particles, energy and momentum conservation, will improve the resolution. A further constraint of interest would require the momentum of the reconstructed B meson to be parallel to the vector pointing from the primary to the secondary vertex (pointing constraint).
As an example, consider the decay $B_s \rightarrow J/\psi\ \phi \rightarrow K^+K^-\mu^+\mu^-$. The invariant mass of the four tracks after the vertex fit but without any additional constraint is shown in Fig. 6.21. The distribution has a Gaussian width of about 40 MeV and the average mass is displaced by some 13 MeV compared to the table value. This is due to the large error on the muon momentum measurement in the CMS detector.
However, the invariant mass distribution becomes significantly narrower and correctly centered when the four-momentum of the two-muon system is constrained to match the J/ψ mass (Fig. 6.22). This constraint is applicable due to the very small width of the J/ψ compared to the measurement uncertainties of typically 10 MeV.

[1] R. H. Richter *et al.*, Nucl.Instr.Meth.**A 377** (1996) 412.

[2] C. Amsler *et al.*, Nucl.Instr.Meth.**A 480** (2002) 501.

[3] R. Kaufmann, PhD Thesis, Universität Zürich, 2001.

[4] B. Henrich and R. Kaufmann, Nucl.Instr.Meth.**A 477** (2002) 304.

[5] V. Bartsch *et al.*, Nucl.Instr.Meth.**A 478** (2002) 330.
V. Bartsch *et al.*, Nucl.Instr.Meth.**A 497** (2003) 389.

[6] M. Barbero *et al.*, Nucl.Instr.Meth.(in print).

[7] R. Frühwirth, K. Prokofiev, T. Speer, P. Vanlaer and W. Waltenberger, Nucl.Instr.Meth.**A 502** (2003) 699.

[8] A. Dorokhov *et al.*, to appear in Nucl.Instr.Meth.**A** preprint physics / 0311050;
T. Rohe *et al.*, submitted to IEEE-TNS 7, preprint physics / 0312009.

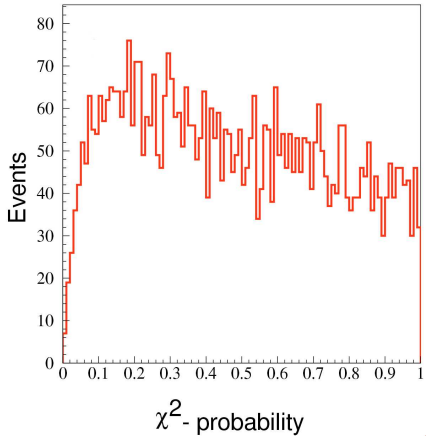

Figure 6.20: *χ^2-probability distribution for the GSF (see text).*

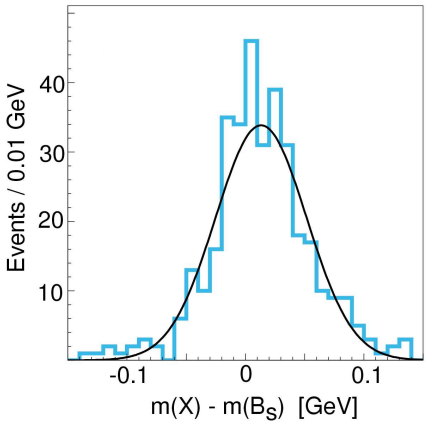

Figure 6.21:
$K^+K^-\mu^+\mu^-$ invariant mass in $B_s \rightarrow J/\psi\ \phi \rightarrow K^+K^-\mu^+\mu^-$ without J/ψ mass constraint.

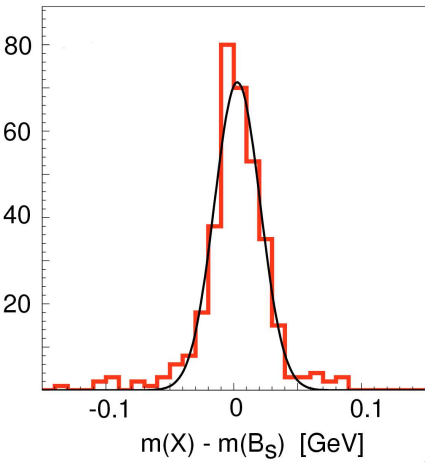

Figure 6.22:
Distribution as in Fig.6.21 but with J/ψ mass constraint.